CrossMark

Long-period Jovian Tilts the Orbits of Two sub-Neptunes Relative to Stellar Spin Axis in Kepler-129

Jingwen Zhang (张婧雯)[1] ，Lauren M. Weiss[1] ，Daniel Huber[1] ，Sarah Blunt[2,10] ，Ashley Chontos[1,10] ，
Benjamin J. Fulton[3] ，Samuel Grunblatt[4,5] ，Andrew W. Howard[2] ，Howard Isaacson[6,7] ，Molly R. Kosiarek[8,10] ，
Erik A. Petigura[9] ，Lee J. Rosenthal[2] ，and Ryan A. Rubenzahl[2,10]

[1] Institute for Astronomy, University of Hawai'i, 2680 Woodlawn Drive, Honolulu, HI 96822, USA; jingwen7@hawaii.edu
[2] Department of Astronomy, California Institute of Technology, Pasadena, CA 91125, USA
[3] NASA Exoplanet Science Institute/Caltech-IPAC, 1200 East California Boulevard, CA, USA
[4] American Museum of Natural History, 200 Central Park West, Manhattan, NY 10024, USA
[5] Center for Computational Astrophysics, Flatiron Institute, 162 5th Avenue, Manhattan, NY 10010, USA
[6] 501 Campbell Hall, University of California at Berkeley, Berkeley, CA 94720, USA
[7] Centre for Astrophysics, University of Southern Queensland, Toowoomba, QLD, Australia
[8] Department of Astronomy and Astrophysics, University of California, Santa Cruz, CA 95064, USA
[9] Department of Physics and Astronomy, University of California Los Angeles, Los Angeles, CA 90095, USA

Abstract

We present the discovery of Kepler-129 d ($P_d = 7.2^{+0.4}_{-0.3}$ yr, $m \sin i_d = 8.3^{+1.1}_{-0.7}\, M_{Jup}$, $e_d = 0.15^{+0.07}_{-0.05}$) based on six years of radial-velocity observations from Keck/HIRES. Kepler-129 also hosts two transiting sub-Neptunes: Kepler-129 b ($P_b = 15.79$ days, $r_b = 2.40 \pm 0.04\, R_\oplus$) and Kepler-129 c ($P_c = 82.20$ days, $r_c = 2.52 \pm 0.07\, R_\oplus$) for which we measure masses of $m_b < 20\, M_\oplus$ and $m_c = 43^{+13}_{-12}\, M_\oplus$. Kepler-129 is a hierarchical system consisting of two tightly packed inner planets and a massive external companion. In such a system, two inner planets precess around the orbital normal of the outer companion, causing their inclinations to oscillate with time. Based on an asteroseismic analysis of Kepler data, we find tentative evidence that Kepler-129 b and c are misaligned with stellar spin axis by $\gtrsim 38°$, which could be torqued by Kepler-129 d if it is inclined by $\gtrsim 19°$ relative to inner planets. Using N-body simulations, we provide additional constraints on the mutual inclination between Kepler-129 d and inner planets by estimating the fraction of time during which two inner planets both transit. The probability that two planets both transit decreases as their misalignment with Kepler-129 d increases. We also find a more massive Kepler-129 c enables the two inner planets to become strongly coupled and more resistant to perturbations from Kepler-129 d. The unusually high mass of Kepler-129 c provides a valuable benchmark for both planetary dynamics and interior structure, since the best-fit mass is consistent with this $2.5\, R_\oplus$ planet having a rocky surface.

Unified Astronomy Thesaurus concepts: Radial velocity (1332); Asteroseismology (73); Exoplanet dynamics (490)

Supporting material: machine-readable table

1. Introduction

Our solar system is a multiplanet system, in which planets orbit in the solar equatorial plane with only a few degrees dispersion. The alignment between solar spin and planetary orbital axes is considered to result from the protoplanetary disk where these planets formed and has been maintained throughout the history of the solar system (Kant 1755; de Laplace 1796). On the contrary, spin–orbit misalignment has been found in dozens of exoplanet systems (e.g., Winn et al. 2010; Huber et al. 2013; Bourrier et al. 2018; Yee et al. 2018; Kamiaka et al. 2019; Rubenzahl et al. 2021), suggesting a different formation pathway or the occurrence of dynamical events in those systems. Measuring the spin–orbit angle therefore helps to understand the formation and evolution of planetary systems. The measurement of spin–orbit misalignment can be achieved by the Rossiter–McLaughlin (RM) effect, which is based on monitoring the sequential distortion in stellar radial velocity (RV) during a planetary transit (McLaughlin 1924; Rossiter 1924; Winn et al. 2005). Similarly, when the stellar lines are sufficiently broadened from rotation, it is possible to spectrally resolve the "shadow" of the planet occulting a specific part of the line in what is

called the Doppler shadow technique (Collier Cameron et al. 2010). The shape of distorted RVs or rotationally broadened spectral lines depends on the spin–orbit angle projected in the sky plane. Because the sizes of the RM effect and Doppler shadow scale with the squared planet radius, they have mostly been used for hot Jupiters. It is much more difficult to apply this technique for super-Earth sized planets.

Another way to probe the spin–orbit misalignment is through asteroseismology (Gizon & Solanki 2003). The stellar rotation induces splittings in oscillation modes that can be used to measure the direction of the stellar spin axis relative to the line of sight. When the host star has transiting planets with nearly edge-on orbits, the difference in inclination between the star and planetary orbits can be obtained (Chaplin et al. 2013). Because the asteroseismic method depends on the stellar parameters but not on the planet size, it can be used to measure the spin–orbit angle in systems with smaller planets. A small but growing number of close-in transiting super-Earths and sub-Neptunes have been observed to possess spin–orbit misalignment (e.g., Huber et al. 2013; Bourrier et al. 2018; Kamiaka et al. 2019). For example, Kepler-56 b and c are two small transiting planets that orbit in a plane inclined with respect to the stellar equator by $\sim 37°$ (Huber et al. 2013).

---
[10] NSF Graduate Research Fellow.

Table 1
Kepler-129 RVs

Time (BJD−2450000)	RV (m s^{-1})	σ_{RV} (m s^{-1})	S_{HK}	Inst
6912.968	−52.65	3.00	0.1256	HIRES
8263.903	67.70	2.02	0.1320	HIRES
8302.092	77.14	2.54	0.1292	HIRES
8329.813	57.54	2.14	0.1317	HIRES
8337.042	49.42	2.19	0.1301	HIRES
…	…	…	…	…

Note. Times are in BJD–2450000.0. The RV uncertainties do not include RV jitter.

(This table is available in its entirety in machine-readable form.)

Several theories have been proposed to explain spin–orbit misalignments in systems with close-in super-Earths or sub-Neptunes. One recently proposed mechanism is that close-in small planets are tilted by a rapidly rotating young star that is highly oblate (Spalding & Batygin 2014; Spalding & Millholland 2020). If the star is misaligned with respect to its protoplanetary disk by some mechanism such as torquing from another star or star-disk magnetic torques, it might tilt the orbits of close-in planets or even excite mutual inclinations between the planets. Another possible mechanism is that planets formed in warped protoplanetary disks and intrinsically possess mutual inclination relative to each other, although observations of disk warps are currently limited (Zanazzi & Lai 2018).

Both of the above scenarios occur in the early age of the system. Alternatively, close-in super-Earths or sub-Neptunes could be aligned with stellar spin when they are formed, but are later tilted out of alignment by an inclined outer giant planet. This scenario requires a nonzero mutual inclination between the inner small planets and outer giant planet(s), which could be caused by dynamical events such as planet–planet scattering (Chatterjee et al. 2008). An example in favor of this scenario is HAT-P-11, which hosts a transiting planet with a projected spin–orbit angle of ∼100° (Winn et al. 2010; Hirano et al. 2011). Yee et al. (2018) later discovered an eccentric outer giant planet ($e \approx 0.6$) in HAT-P-11 and proposed that the misalignment could be caused by nodal precession of the inner orbit around that of the outer giant's orbit. Using Gaia DR2 and Hipparcos astrometry, Xuan & Wyatt (2020) measured a mutual inclination of >54° (1σ) between the two planets in HAT-P-11, which supports this picture. In addition, the transiting super-Earth and giant planet in π Men were found to be mutually inclined by ∼50° (Xuan & Wyatt 2020; Damasso et al. 2020; De Rosa et al. 2020). Soon after, the super-Earth in π Men was found to be moderately misaligned with the stellar spin axis by ∼30° with the Doppler shadow technique (Kunovac Hodžić et al. 2021).

So far, direct measurements of mutual inclination between inner small planet and outer giant planets are still limited to a few systems. Indirect methods can be used to set a constraint on the mutual inclination. For example, based on the number of transiting giant planets in Kepler systems that also host transiting super-Earths, Masuda et al. (2020) estimated the average mutual inclination between inner super-Earths and outer giant planets to be around $11°.8^{+12.7}_{-5.5}$ (1σ confidence). In addition, an inclined outer perturber may increase mutual inclinations between the inner planets or even destabilize their orbits (Becker & Adams 2017; Huang et al. 2017;

Lai & Pu 2017; Pu & Lai 2018; Denham et al. 2019). Thus, if a system hosts two or more transiting planets, the double-transit probability can provide an upper boundary for the mutual inclination between the inner small planets and outer giant planets (e.g., Becker & Adams 2017).

Kepler-129 (KOI-275) hosts two transiting planets, Kepler-129 b and c, which are sub-Neptunes with orbital periods of 15.79 days and 82.20 days, respectively (Rowe et al. 2014; Van Eylen & Albrecht 2015). We report the discovery of a long-period giant planet (hereafter Kepler-129 d) based on RV observations with the Keck/HIRES spectrograph and study the interaction between inner small planets and the outer giant planet in this system.

2. Observations

2.1. System Parameters

Kepler-129 is a subgiant G4V star at an age of $6.43^{+0.64}_{-0.61}$ Gyr at a distance of $402.73^{+12.28}_{-12.43}$ pc (Silva Aguirre et al. 2015). The measured mass is $1.178^{+0.021}_{-0.030} M_\odot$, the radius is $1.653^{+0.009}_{-0.012} R_\odot$, and [Fe/H] is 0.29 ± 0.10 (Silva Aguirre et al. 2015; Fulton & Petigura 2018). Its projected rotation velocity $v \sin i$ determined spectroscopically is 2.13 ± 1.0 km s^{-1} (Petigura 2015). The system has two transiting planets, Kepler-129 b and c, which are two sub-Neptunes ($r_b = 2.40 \pm 0.04\ r_\oplus$, $r_c = 2.52 \pm 0.07\ r_\oplus$) with orbital periods of 15.79 and 82.20 days and eccentricities of $0.01^{+0.24}_{-0.01}$ and $0.20^{+0.15}_{-0.20}$, respectively (Rowe et al. 2014; Van Eylen & Albrecht 2015). The stellar and planetary parameters are given in Table 2.

2.2. Keck/HIRES Radial Velocities

We collected the RV data for Kepler-129 from 2014 to 2021 using the High Resolution Echelle Spectrometer (HIRES, $R \sim 60,000$; Vogt et al. 1994) at the W.M. Keck Observatory. The observations are part of the Kepler Giant Planet Survey, which aims to search for long-period giant planets around 60 Kepler stars with HIRES (L. M. Weiss et al. 2021, in preparation). The observation setup is the same as that used by the California Planet Search (Howard et al. 2010). We used the C2 decker (0″.86 × 14″) to subtract the contaminating light from the sky background. The wavelength calibration was done with a iodine gas cell in the light path. A iodine-free template spectrum bracketed by observations of rapidly rotating B-type stars was used to deconvolve the stellar spectrum from the spectrograph point-spread function. We then forward model the spectra taken with the iodine cell using the deconvolved template spectra. The wavelength scale, instrumental profile, and RV in each of the ∼700 segments of 80 pixels were solved simultaneously (Howard et al. 2010). Our Keck-HIRES RVs are presented in Table 1.

2.3. Kepler Photometry

We used Kepler short cadence time series ($\Delta t \sim 58.85$ s) to detect the solar-like oscillations of Kepler-129 with a typical period of a few minutes. The available short cadence data for Kepler-129 consists of two parts, one spans from Q6.1–Q7.3 (2010 June 24–December 22) and another was collected during Q17.1 and Q17.2 (2013 April 9–May 11). We reduced the data with the *lightkurve* (Lightkurve Collaboration et al. 2018) package. The frequency-power spectra were computed using a Lomb–Scargle periodogram (Scargle 1982). In order to avoid

the window effect due to the long gap between Q6/Q7 and Q17, we removed it from the light curves by making the Q17 timestamps consecutive with those of Q7. The process is justified since the oscillations are not phase coherent and the length of the gap is much larger than the period and mode lifetime of the oscillations (Hekker et al. 2010).

3. Keplerian Fit

3.1. Maximum Likelihood Fitting

The RVs of Kepler-129 reveal a long term variation from a planetary companion, and the single data point collected in 2014 provides a constraint that the long period is approximately 3000 days. We used *RadVel* (Fulton et al. 2018), a Keplerian multiplanet RV fitting package, to obtain orbital properties for all three planets. Keplerian orbits are fitted with five orbital elements K, $\ln P$, T_{conj}, $\sqrt{e}\sin\omega$, $\sqrt{e}\cos\omega$, where K is the RV semiamplitude, P is the orbital period, T_{conj} is the time of conjunction, e is the eccentricity, and ω is the argument of pericenter. In addition, a HIRES RV zero-point γ and a RV jitter term σ are fitted in the models. We fix the orbital periods and times of conjunction of the two inner planets Kepler-129 b and c since they are well determined by Kepler observations (Van Eylen & Albrecht 2015). We also set their eccentricity and argument of pericenter as 0 to simplify the fitting as they are likely to have low eccentricities (Van Eylen & Albrecht 2015). Therefore, for the two inner planets, the only free parameters are their K amplitudes. For the outer giant planet, we allow all five of its orbital parameters to vary. In addition, we set bounds on $0 < e < 1$, $K > 0$, $0 < \sigma < 10$ for all planets. The set of orbital parameters was determined based on minimum χ^2 fitting. Figure 1 shows the best-fit Keplerian solution.

3.2. Parameter Uncertainties with MCMC

We performed the Markov chain Monte Carlo (MCMC) exploration with emcee (Foreman-Mackey et al. 2013) to estimate parameter credible levels. Our MCMC analysis used 50 walkers and ran for $\sim 10^4$ steps per walker, achieving a maximum Gelman–Rubin statistic of 1.005. We derived the (minimum) planet mass from RV amplitudes ($m_b < 20\,M_\oplus$ (95%), $m_c = 43^{+13}_{-12}\,M_\oplus$, $m\sin i_d = 8.3^{+1.1}_{-0.7}\,M_{\mathrm{Jup}}$). The derived planetary parameters are given in Table 2.

Figure 2 shows that the minimum mass distribution of Kepler-129 d has a tail beyond 13 M_{Jup}, which is the traditional boundary between planet and brown dwarf based on deuterium burning limit (Grossman & Graboske 1973). Given that the $\sin i_d$ is unknown, the true mass of Kepler-129 d could be larger, possibly pushing it into brown dwarf regime under this definition. On the other hand, several studies argue for the formation-based definition that planets form through core accretion and brown dwarfs form due to gravitational instability (Schlaufman 2018). The formation channels predict two patterns: objects formed through core accretion are preferentially found around metal-rich stars and with low eccentricity, whereas those formed through gravitational collapse occur with equal efficiency independent of stellar metal abundance and tend to have larger eccentricity (Schlaufman 2018; Bowler et al. 2020). Our results of the low eccentricity ($e_d = 0.15^{+0.07}_{-0.05}$) of Kepler-129 d, as well as the high metal abundance of the star ([Fe/H] ~ 0.26), is consistent with a planet definition, although we cannot rule out the possibility of the brown dwarf. For the sake of simplicity, we will refer to Kepler-129 d as a giant planet in this paper.

Figure 3 shows the masses and radii of Kepler-129 b and c in comparison to the masses and radii of other sub-Neptunes from NASA Exoplanet Archive. We only selected planets with mass uncertainties $\sigma_M/M < 25\%$. The mass range of Kepler-129 b overlaps with the predicted mass at 2.4 $R_\oplus$ using the mass–radius relation in Weiss & Marcy (2014). It likely consists of a rocky/iron core and a gaseous H/He envelope (Lopez & Fortney 2014). Kepler-129 c has a unique high mass, significantly (3σ) above the Weiss & Marcy (2014) mass and radius relationship; although it has nearly the same radius with Kepler-129 b. To better constrain the mass of Kepler-129 c, more RVs are needed. The high mass of Kepler-129 c indicates it may be a rocky core without atmosphere. Although Kepler-129 b and c likely formed in a similar environment, they have very different masses; the reason for which is unclear but would be interesting for studies of planet composition and formation. For comparison, we identified seven other planets with high masses in Figure 3. Five of them (blue squares), measured by Xie (2014) using the TTV method, have relatively large uncertainties due to the degeneracy between planet mass and orbital eccentricity. The mass of the other two planets, TOI-849 b (purple square) and HD 95338 b (red square), are better constrained with RV observations. TOI-849 b, with an ultrashort orbital period of <1 day, is considered as a remnant core of a giant planet (Armstrong et al. 2020). HD 95338 b, with an orbital period of $\sim$55 days, could be a Neptune-sized planet with a dense atmosphere (Díaz et al. 2020). If its high mass is confirmed, Kepler-129 c would be the most massive rocky planet discovered yet.

4. Asteroseismic Analysis

Kepler-129 is a hierarchical system consisting of tightly packed inner planets and an external companion. The inner planetary system may be disturbed by the outer giant planet. One aspect that could shed light on the system's dynamical history is the evolution of the angle between the stellar spin axis and the total orbital angular momentum of the inner planetary system, namely the spin–orbit angle. Unless otherwise specified, we always define the spin–orbit angle with respect to the inner planetary system in this paper. Campante et al. (2016) measured the spin–orbit angle of Kepler-129 with asteroseismology, but only consider Kepler data collected in Q6/7. In this section, we present our measurements of the spin–orbit angle based on the asteroseismic analysis using Kepler data collected in Q6/7 and Q17.

4.1. Principles of the Method

Solar-like oscillations are acoustic global standing waves stochastically excited and damped by near-surface convections, and they enable measurements of the angle between the stellar spin axis and light of sight, i_s (Gizon & Solanki 2003; Ballot et al. 2006, 2008; Campante et al. 2011, 2016). The oscillation modes, characterized by the radial order n, the spherical degree l, and the azimuthal order m, are typically observed in the frequency-power spectrum showing a pattern of peaks with near-regular frequency separations (Vandakurov 1967). Figure 4 shows the power spectra of the light curves of Kepler-129, presenting clear patterns of
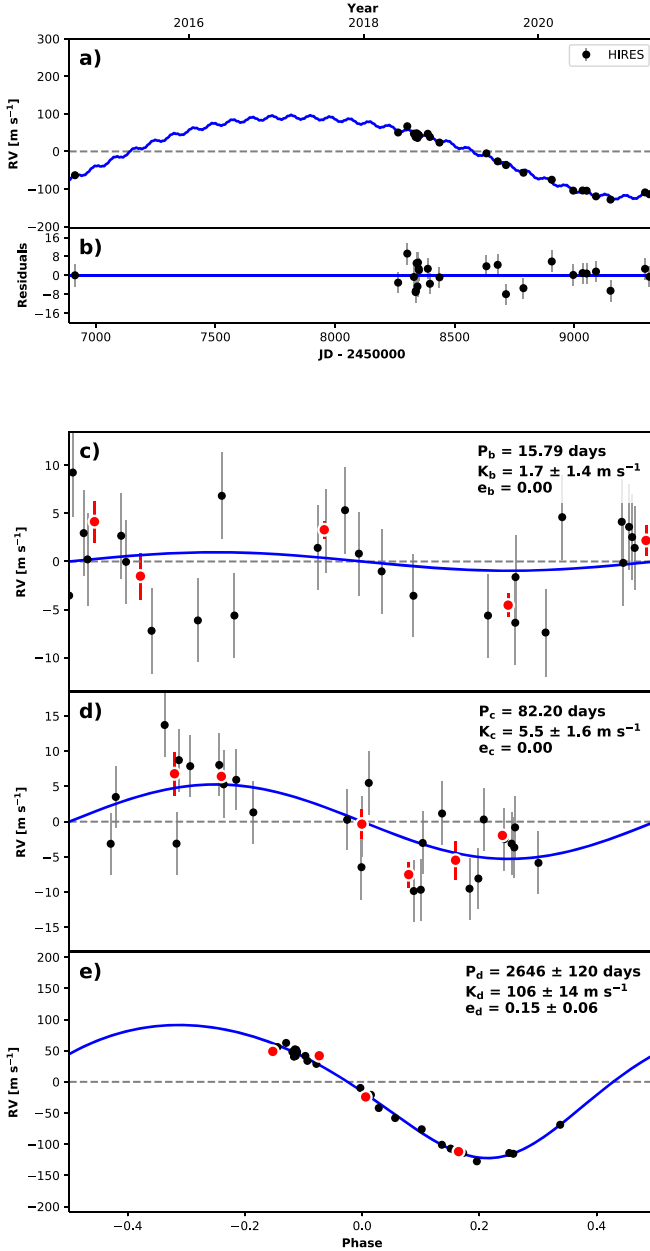
Figure 1. Best-fit 3-planet Keplerian orbital model for Kepler129. (a): Kepler-129 RVs with errors (black) and their best-fit model (blue) as a function of time. (b): the residuals. (c) ∼ (e): RV data and models for each planet phase folded at the best-fit orbital period with all other planets' signals removed. The orbital periods, time of conjunction, and eccentricities for planet b and c are fixed since they are well constrained from transit observations.

Table 2
Stellar and Planetary Properties

Parameter	Credible Interval	Units	References
Stellar Parameters			
$T_{\rm eff}$	5770 ± 83	K	A
$M_\star$	$1.178^{+0.021}_{-0.030}$	$M_\odot$	A
$R_\star$	$1.653^{+0.009}_{-0.012}$	$R_\odot$	A
[Fe/H]	0.29 ± 0.10	dex	A
$v \sin i$	2.13 ± 1	km s^{-1}	D
Age	$6.43^{+0.64}_{-0.61}$	Gyr	A
k_2	0.001		C
C	0.05	$M_\star R_\star^2$	C
Stellar Inclination	52^{+10}_{-13}	deg	This work
Kepler-129 b			
r_b	2.40 ± 0.04	$R_\oplus$	B
P_b	15.79	days	B
a_b	0.13	au	B
$T_{\rm conjb}$	2454978.2	JD	B
K_b	$< 4.5(95\%)$	m s^{-1}	This work
m_b	$< 20(95\%)$	$M_\oplus$	This work
ρ_b	$<8.1\ (95\%)$	g cm^{-3}	This work
Kepler-129 c			
r_c	2.52 ± 0.07	$R_\oplus$	B
P_c	82.20	days	B
a_c	0.39	au	B
$T_{\rm conjc}$	2455041.8	JD	B
K_c	5.5 ± 1.6	m s^{-1}	This work
m_c	43^{+13}_{-12}	$M_\oplus$	This work
ρ_c	14.8 ± 4.3	g cm^{-3}	This work
Kepler-129 d			
P_d	2646^{+140}_{-94}	days	This work
a_d	4.0 ± 0.1	au	This work
$T_{\rm conjd}$	2458637^{+42}_{-70}	JD	This work
K_d	106^{+17}_{-10}	m s^{-1}	This work
e_d	$0.15^{+0.07}_{-0.05}$		This work
w_d	$-3.0^{+0.8}_{-1.0}$	radians	This work
$m \sin i_d$	$8.3^{+1.1}_{-0.7}$	$M_{\rm Jup}$	This work
Other Parameters			
σ	$5.0^{+1.2}_{-1}$	m s^{-1}	This work
γ	14^{+19}_{-13}	m s^{-1}	This work
$\dot{\gamma}$	$\equiv 0$		This work
$\ddot{\gamma}$	$\equiv 0$		This work

Note. A: Silva Aguirre et al. (2015); B: Van Eylen & Albrecht (2015); C: Landin et al. (2009); D: Petigura (2015). k_2 is the stellar second fluid Love number and C is the stellar moment of inertia along the short axis. Intervals are 68% credible unless stated otherwise.

peaks from solar-like oscillations near 1300 μHz. The overtones of radial ($l = 0$) and low-order nonradial ($l = 1$) modes are detectable.

The asteroseismic determination of i_s is based on resolving the rotational splitting of modes in the power spectra. Rotation introduces a dependence of oscillation frequencies of nonradial modes on m, with prograde ($m > 0$) and retrograde ($m < 0$) modes having frequencies slightly higher or lower than the axisymmetric mode ($m = 0$) in the observer's frame of reference (Gizon & Solanki 2003; Chaplin & Miglio 2013). For stars assumed to rotate as a solid body with angular velocity $v_\star$, the frequency ν_{nlm} can be expressed to first order as (Ledoux 1951):

$$\nu_{nlm} = \nu_{nl0} + m\frac{v_\star}{2\pi}(1 - C_{nl}) \approx \nu_{nl0} + m\delta\nu_s \qquad (1)$$

where C_{nl} is the dimensionless Ledoux constant to correct the effect of the Coriolis force and $C_{nl} \ll 1$ for high-order modes (large n) so that the rotational splitting can be given approximately by the stellar angular velocity, $\delta\nu_s \approx v_*/2\pi$.

The dependence of mode power on m can be written as (Dziembowski 1977; Gizon & Solanki 2003):

$$\varepsilon_{lm}(i_s) = \frac{(l - |m|)!}{(l + |m|)!}[P_l^{|m|}(\cos(i_s))]^2 \qquad (2)$$

where $P_l^{|m|}(x)$ are the associated Legendre functions and the sum of $\varepsilon_{lm}(i_s)$ over m has been normalized to unity. Hence,
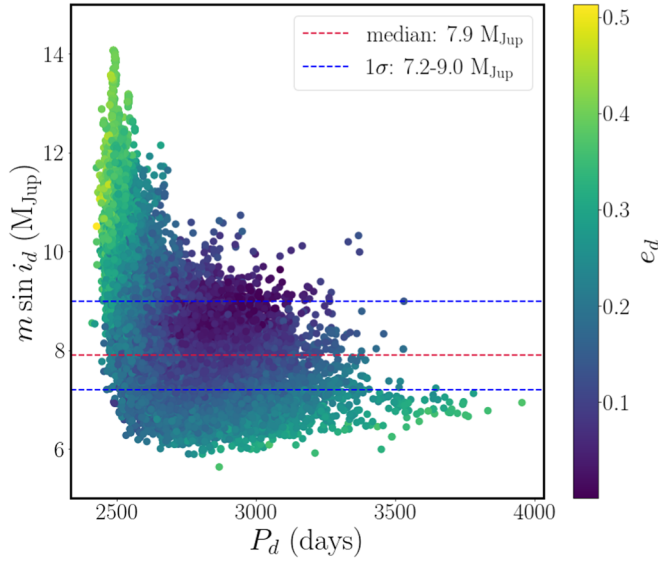
Figure 2. The minimum mass of Kepler-129 d as a function of the orbital period colored by eccentricity. The red-dashed line corresponds to median value of $m\sin i$ and the blue-dashed lines indicate the 1σ confidence interval. Kepler-129 d is a massive long-period giant planet with low eccentricity, whose minimum mass distribution has a tail beyond the traditional boundary between planets and brown dwarfs based on the deuterium burning limit (13 $M_{\rm Jup}$).
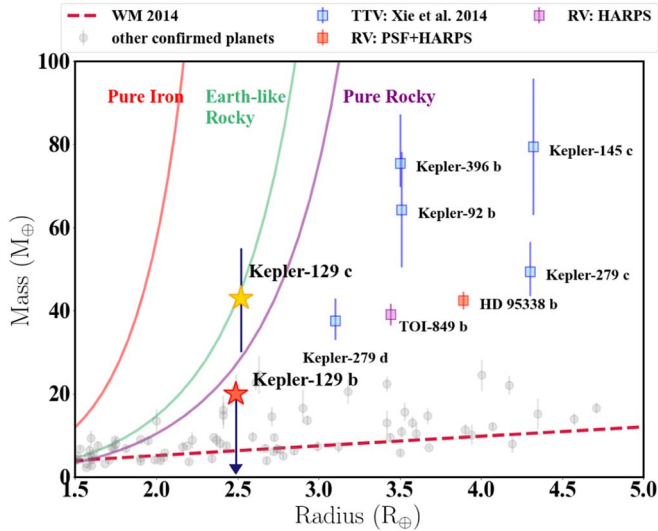

Figure 4. Power spectrum of Kepler-129. Top panel: log-scale frequency-power spectra using Lomb–Scargle periodogram. The light gray lines are original spectra, whereas red lines show the spectra after smoothing with a 1.0 μHz filter. Dark blue region indicates the oscillation bump. Bottom panel: same as top panel, but in the frequency range of the oscillation bump. $l = 0,1$ modes are marked. The green line shows the best-fitting model from Campante et al. (2016). Kepler-129 presents clear solar-like oscillations, appearing as a pattern of evenly spaced peaks in the Frequency-power spectra.

Figure 3. Mass vs. radius for Kepler-129 b and c in comparison to other confirmed planets from NASA Exoplanet Archive. The plotted planets have orbital periods smaller than 100 days, radius between 1.5 $R_\oplus$ and 5 $R_\oplus$, and <25% mass uncertainty. The solid lines are planet composition lines from Zeng & Seager (2008). The red dashed line corresponds to the mass–radius relation given by Weiss & Marcy (2014). The mass range of Kepler-129 b overlaps with the Weiss & Marcy (2014) relation, which suggests the possibility of Kepler-129 b having an H/He envelope. Kepler-129 c has a unique high mass, indicating it may be a rocky core without atmosphere.

measuring the relative power of the azimuthal components in a nonradial multiplet provides a direct estimate of the stellar inclination angle i_s.

4.2. Estimation of the Stellar Inclination

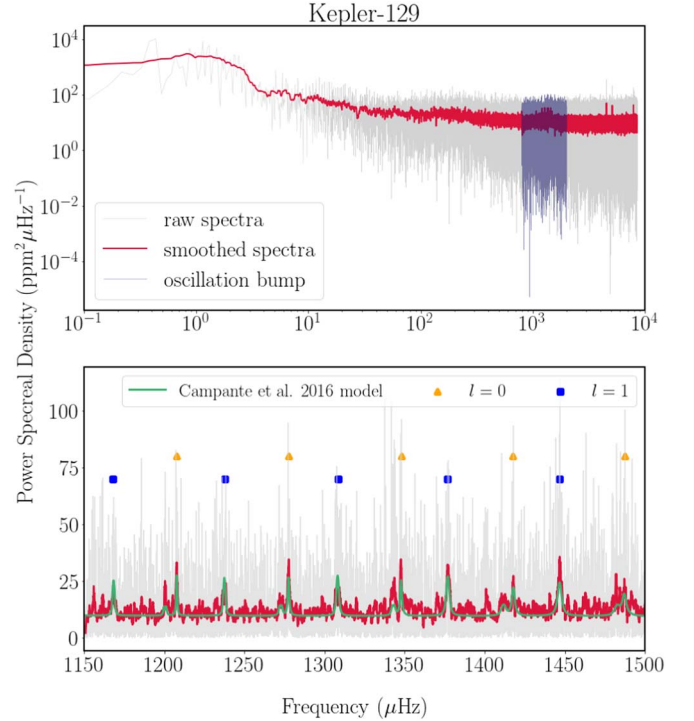Figure 5 shows the five strongest dipole modes ($l = 1$) in the oscillation spectrum of Kepler-129. We modeled the oscillations using a superposition of Lorentzian functions:

$$\mathcal{P}(\nu) = \sum_n \sum_{m=-l}^{l} \frac{\varepsilon_{lm}(i_s) H_{nlm}}{1 + 4\left[\frac{\nu - \nu_{nl0} - m\delta\nu_s}{\Gamma_{nlm}}\right]^2} + \mathcal{B}(\nu) \quad (3)$$

where H_{nlm} and Γ_{nlm} are the height and width of the Lorentzian profiles corresponding to every m component ($m = -1, 0, 1$ when $l = 1$). $\mathcal{B}(\nu)$ describes the background terms coming from granulations, stellar activities, and photon noise. The inner sum runs over the m components of each rotationally split multiplet, while the outer sum runs over all observed modes, in radial order n. Note that we consider five most significant dipole modes that ($n = 15, 16, 17, 18, 19; l = 1$).

We use an MCMC algorithm to fit all five observable modes simultaneously. The central frequency ν_{nl0} and mode height H_{nlm} for are fitted for each mode, while the angle $\cos i_s$, linewidth Γ_{nlm}, rotational splitting $\delta\nu$, and noise floor $\mathcal{B}(\nu)$ are assumed to be the same for all five modes. Hence, the fitting includes a total of 14 parameters. We adopt Jeffreys prior for the mode heights and uniform priors for all other parameters with boundaries of $0 < \cos i_s < 1$, $0 < \delta\nu < 10$, $0 < \Gamma_{nlm} < 10$ and $H_{nlm} > 0$. Note that we uniformly sample in $\cos i_s$, which corresponds to an isotropic spin distribution.

We use 50 walkers and performed 10^4 iterations with each walker. The first 10% of each chain is discarded for burn-in. Figure 6 presents the joint posterior distribution of Γ, $\cos i_s$ and $\delta\nu$. The MCMC fitting shows the best-fitting values of $\cos i_s = 0.62^{+0.13}_{-0.18}$, $\Gamma = 0.63^{+0.42}_{-0.20}$ μHz, and $\delta\nu =$
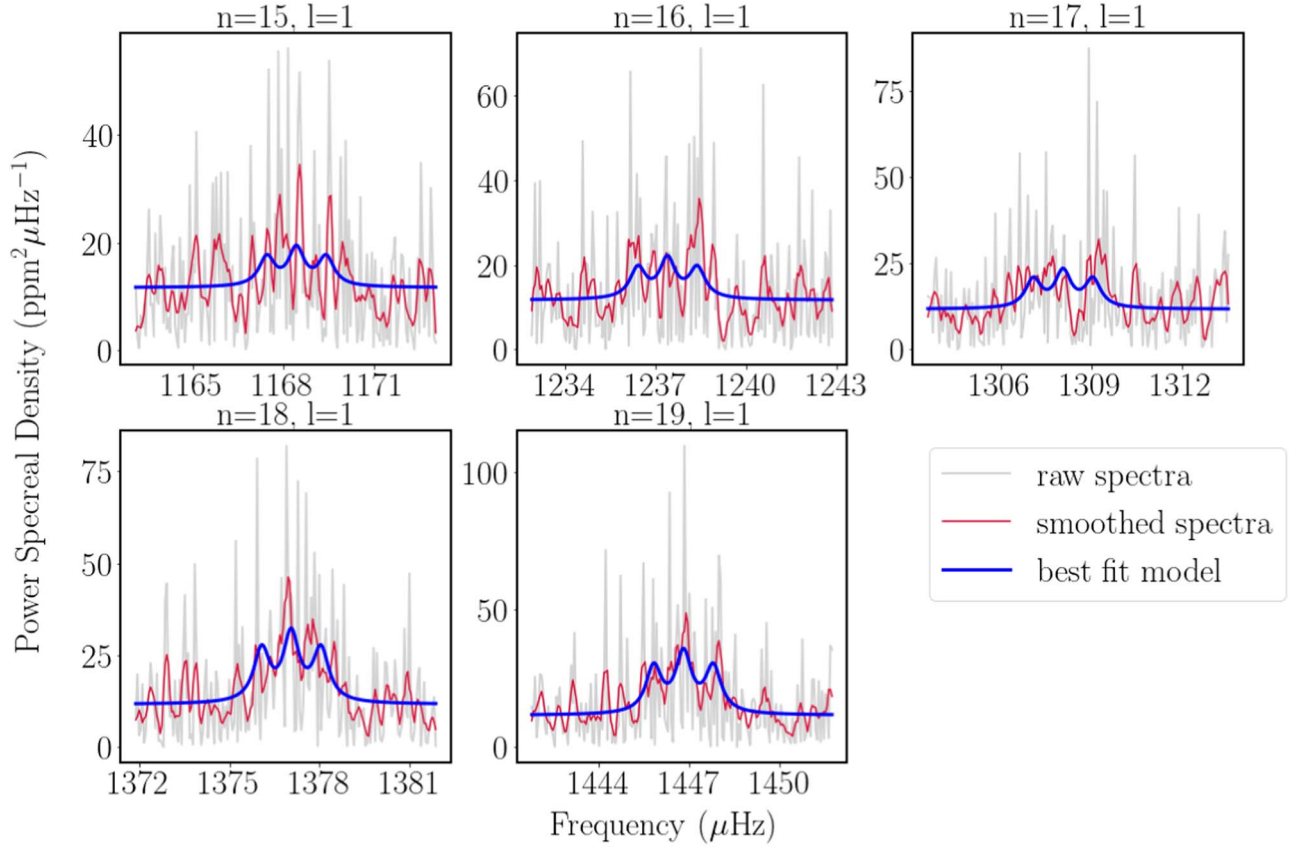
Figure 5. The rotational frequency splitting in five $l = 1$ modes. Light gray lines: original spectra. Red lines: the spectra after smoothing with a 0.2 μHz. Blue lines: our best-fit MCMC model. Note that not all observed modes are expected to show clear splitting due to the stochastic nature of the oscillations.
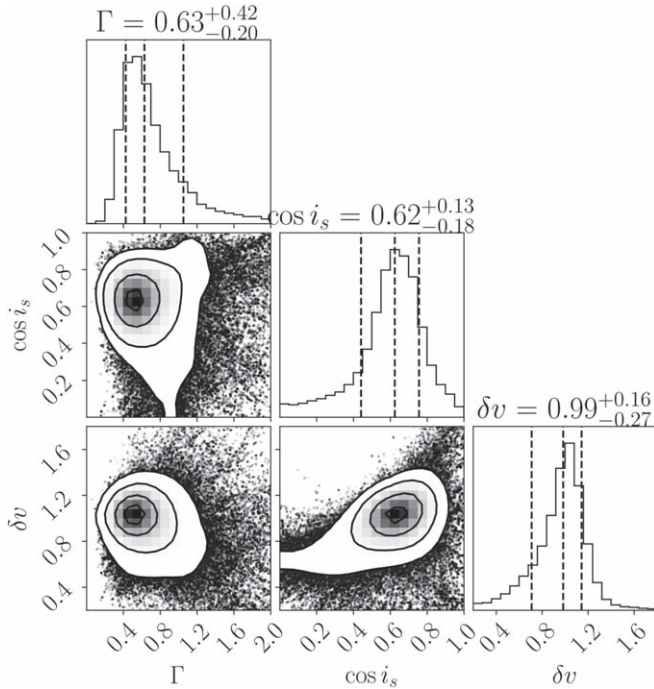

Figure 6. Joint posterior distributions for the Γ, i_s, and $\delta\nu$ from MCMC fitting. Moving forward, the solid lines correspond to 1σ, 2σ, and 3σ contours. The MCMC fitting converges at $\Gamma \sim 0.63$ μHz, $\cos i_s \sim 0.62$ ($i_s \sim 52°$), and $\delta\nu \sim 0.99$ μHz, indicating the misalignment between stellar spin axis and orbital axes of the transiting planets Kepler-129 b and c. Our results show the data disfavor the spin–orbit alignment: ($i_s = 90°$).

$0.99^{+0.16}_{-0.27}$ μHz. Hence we obtained $i_s = 52^{+10}_{-13}$ deg. The best-fitting values and uncertainties were calculated as the median and 1σ interval of the marginalized posterior distribution for each parameter. Our results show the data disfavor the spin–orbit alignment ($i_s = 90°$) with 2σ confidence.

Our results are consistent with that found by Campante et al. (2016; $i_s = 50^{+36.6}_{-15.6}$ deg at 1σ confidence), but have smaller uncertainties. We obtain a larger ratio $\delta\nu/\Gamma$ than that in Campante et al. (2016) ($\delta\nu/\Gamma \sim 0.6$). The both measured linewidth Γ are consistent with the expected range ($0.9^{+0.4}_{-0.4}$ μHz) at the effective temperature of Kepler-129 given by Lund et al. (2017). Kamiaka et al. (2018) also measure the frequency splitting of Kepler-129 using Kepler data collected during Q6–Q7. They obtained a consistent result of $i_s = 42.9^{+26.6}_{-23.2}$ deg (1σ) and $\delta\nu/\Gamma \sim 0.95$. Note that they categorize Kepler-129 as a star for which seismic inclinations are difficult to measure and hence our value should be used with some caution. However, given that we include more data collected during Q17 and there are two independent studies with similar results, we are confident about our results. In addition, using the stellar radius from Silva Aguirre et al. (2015) and the rotation frequency $\delta\nu$ from our MCMC fitting, we estimated stellar rotation velocity v of $7.2^{+1.2}_{-1.9}$ km s^{-1}, which is significantly larger than projected velocity $v \sin i$ of 2.13 ± 1 km s^{-1} measured from stellar spectra (Petigura 2015). This indicates that $\sin i$ is much smaller than one and is consistent with our measurements of $i_s < 90°$.

4.3. Limits on the Spin–Orbit Angle

Measurements of i_s, along with the angle between the planet's orbital axis and line of sight (i_0) and the sky-projected spin–orbit angle (λ), can be used to compute the true spin–orbit angle ψ as (Fabrycky & Winn 2009)

$$\cos\psi = \sin i_s \cos\lambda \sin i_0 + \cos i_s \cos i_0. \qquad (4)$$

The angle i_0 of a transiting planet is approximately 90° given its nearly edge-on orbit. In principle, The sky-projected spin–orbit angle λ can be obtained with measurements of the Rossiter–McLaughlin effect, although this angle is difficult to constrain for small planets. Based on our measurement of $i_s \sim 52°$ and assuming $i_0 = 90°$ for the transiting planets Kepler-129 b and c, the lower limit for the true spin–orbit angle ψ can be approximated with Equation (4) when λ is unknown:

$$\cos\psi < \sin i_s \sin i_0 + \cos i_s \cos i_0. \qquad (5)$$

Hence, the true spin–orbit angle between the star and transiting planets should be larger than 38°, indicating a misalignment between the orbital planes of Kepler-129 b and c and the stellar equatorial plane.

5. Orbital Dynamics

The existence of Kepler-129 d offers a natural explanation for the spin–orbit misalignment of the inner planets. If the orbit of Kepler-129 d is inclined with respect to those of the inner planets, it could have imposed a torque on the inners and excited them out of the equatorial plane of the host star. In addition to exciting the spin–orbit angle, an inclined outer giant planet could also excite mutual inclinations between inner planets, possibly preventing them from transiting together (Becker & Adams 2017; Lai & Pu 2017; Read et al. 2017). The fact that we observe both Kepler-129 b and c to be transiting places an additional constraint on the inclination of Kepler-129 d. In other words, the inclination of d must be large enough that a spin–orbit angle of $\sim38°$ can be produced, while small enough that both planets b and c have a large probability of transiting together. In this section, we investigate the dynamic evolution of both the spin–orbit angle (Section 5.1.1) and the mutual inclination between inner planets (Section 5.1.2).

5.1. Analytical Model

5.1.1. Spin–Orbit Angle Evolution

We apply the results of the "three-vector problem" (Boué & Laskar 2006, 2009; Boué & Fabrycky 2014a, 2014b) to explore how the spin–orbit angle evolves under the influence of an inclined Kepler-129 d. The three-vector problem was developed to model the secular evolution of three coupled angular motions. Here, the three vectors are the angular momentum of the star $L_\star = L_\star \hat{l}_\star$, the total angular momentum of the inner planets $L_{in} = L_{in}\hat{l}_{in}$, and that of the outer giant planet $L_d = L_d \hat{l}_d$, where $\hat{l}_\star$, $\hat{l}_{in}$, $\hat{l}_d$ are unit vectors. In this subsection, we consider the total angular momentum of the inner planetary system L_{in} instead of the two individual planets

$$L_{in} = \sum_{j=b,c} L_j \hat{l}_j = L_{in}\hat{l}_{in} \qquad (6)$$

where $\hat{l}_j$ is the unit vector normal to the orbit of planet j. The three vectors would precess around each other during the

evolution. Following the convention in Boué & Fabrycky (2014b), we denote ν_1, ν_2, ν_3, ν_4 as the precession frequencies of $\hat{l}_\star$ around $\hat{l}_{in}$, of $\hat{l}_{in}$ around $\hat{l}_\star$, of $\hat{l}_{in}$ around $\hat{l}_d$, and of $\hat{l}_d$ around $\hat{l}_{in}$, respectively. They can be estimated using the stellar parameters ($M_\star$, $R_\star$, P_{tot}, k_2, C) and planetary properties and orbital parameters (m_b, m_c, $m\sin i_d$, a_b, a_c, a_d, e_d; see in Boué & Fabrycky 2014b).

We find the Kepler-129 system is consistent with the "Pure Orbital Regime" in Boué & Fabrycky (2014b), with ν_1, ν_2, $\nu_4 \ll \nu_3$. For Kepler-129, we estimate $\nu_1 \approx 1.5 \times 10^{-4}\,\mathrm{deg\,kyr}^{-1}$, $\nu_2 \approx 5 \times 10^{-5}\,\mathrm{deg\,kyr}^{-1}$, $\nu_3 \approx 6.9\,\mathrm{deg\,kyr}^{-1}$, $\nu_4 \approx 0.04\,\mathrm{deg\,kyr}^{-1}$. In this regime, the frequencies associated with the inner planetary system coupling to the stellar spin (ν_1 and ν_2) are much smaller than those associated with the inner planetary system coupling to the outer planet (ν_3 and ν_4). This suggests that the stellar spin would neither significantly influence the orbits of planets nor be affected by the motion of planets. Among the planets, Kepler-129 d contains much more angular momentum than Kepler-129 b and c, so its orbital plane is almost invariant ($\nu_4 \ll \nu_3$). Therefore, the dominant evolution in Kepler-129 is the precession of inner planets around the orbital axis of the outer giant planet at a roughly constant angle. The precession period is $P = 2\pi/\nu_3 \approx 52$ kyr, which is much shorter than the stellar age.

We assume inner planets were aligned with the stellar spin axis when they formed as shown in Figure 7(a). The orbit of Kepler-129 d was inclined by ΔI relative to inner planets possibly due to the warped protoplanetary disk or through dynamical events such as planet–planet scattering. Then Kepler-129 b and c began to precess around Kepler-129 d at a constant angle ΔI. During the inner planets' precession, their spin–orbit angle oscillates over time and reaches the maximum of $2\Delta I$ after half-period's precession (Figure 7(b); Boué & Fabrycky 2014b). Therefore, our measurement of spin–orbit angle ($\sim38°$) in Section 4 requires that Kepler-129 d is inclined relative to Kepler-129 b and c by at least $\sim19°$.

5.1.2. Mutual Inclination between Inner Planets

In this section, we investigate the efficacy with which Kepler-129 d excites mutual inclinations between planet b and c. Here, we neglect the influence of the stellar spin angular momentum as the precession rate of L_{in} around $L_\star$ (ν_2) is much slower than that of L_{in} around L_d (ν_3) as found in Section 5.1.1. In contrast to the above analysis, we now consider the orbital angular momenta of planet b and c separately, and thus have three vectors $L_b = L_b\hat{l}_b$, $L_c = L_c\hat{l}_c$ and $L_d = L_d\hat{l}_d$, where $\hat{l}_b$, $\hat{l}_c$, and $\hat{l}_d$ are unit vectors. Because the angular momentum of Kepler-129 d is much larger than that of Kepler-129 b and c (L_b, $L_c \ll L_d$), $\hat{l}_d$ is hardly affected by L_b and L_c and is approximately fixed. The evolution of $\hat{l}_b$ and $\hat{l}_c$ can be described as their precession around each other and around $\hat{l}_d$ (Lai & Pu 2017)
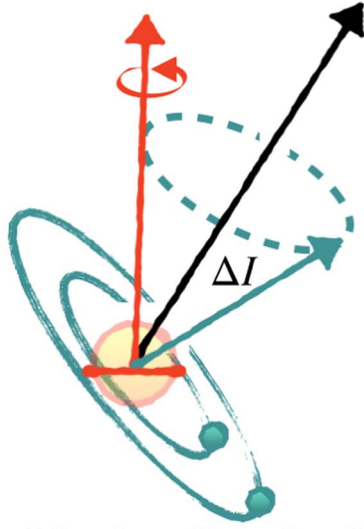
$$\frac{d\hat{l}_b}{dt} = -\nu_{bc}(\hat{l}_b \cdot \hat{l}_c)(\hat{l}_c \times \hat{l}_b) - \nu_{bd}(\hat{l}_b \cdot \hat{l}_d)(\hat{l}_d \times \hat{l}_b) \qquad (7)$$

$$\frac{d\hat{l}_c}{dt} = -\nu_{cb}(\hat{l}_c \cdot \hat{l}_b)(\hat{l}_b \times \hat{l}_c) - \nu_{cd}(\hat{l}_c \cdot \hat{l}_d)(\hat{l}_d \times \hat{l}_c) \qquad (8)$$

where ν_{bc} and ν_{bd} represent the precession rate of $\hat{l}_b$ around $\hat{l}_c$ (driven by Kepler-129 c) and that of $\hat{l}_b$ around $\hat{l}_d$ (driven by
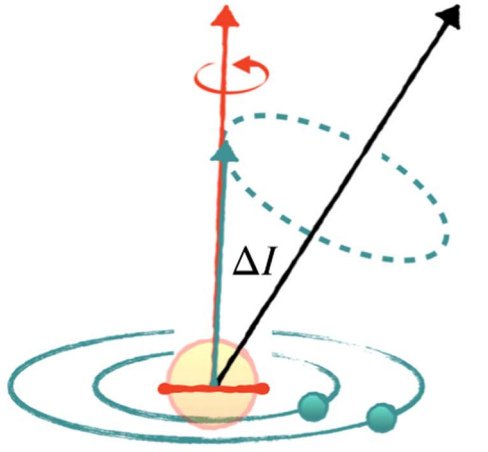
(a) Initial aligned orbits

(b) Maximally misaligned orbits after half-period precession

Figure 7. The spin–orbit angle of Kepler-129 b and c oscillates as their total angular momentum (green vector) precess around that of Kepler-129 d (black vector) at an angle ΔI. ΔI keeps constant during the precession. (a) Initially, the inner planetary system is aligned with the stellar spin axis (red vector), but the outer giant planet is inclined by ΔI relative to them. (b) As the inner planets precess around outer giant planet (along the green-dashed line), they achieve a maximum spin–orbit angle that is $2\Delta I$.

Kepler-129 d). ν_{cb} and ν_{cd} are the precession rates of $\hat{l}_c$ around $\hat{l}_b$ (driven by Kepler-129 b) and around $\hat{l}_d$ (driven by Kepler-129 d). They can be computed using the masses, semimajor axes, and angular momenta of the planets (See Lai & Pu 2017).

Together, these four parameters determine whether the two inner planets dynamically couple with each other. A difference between ν_{bd} and ν_{cd} means that two inner planets precess around the giant planet at different rates, resulting in the separation of $\hat{l}_b$ from $\hat{l}_c$. On the other hand, the precession of Kepler-129 b and c around each other (at rates of ν_{bc} and ν_{cb}) act to keep $\hat{l}_b$ and $\hat{l}_c$ coupled together. Lai & Pu (2017) define the parameter $\epsilon = (\nu_{bd} - \nu_{cd})/(\nu_{bc} + \nu_{cb})$ to estimate the relative coupling strength between the inner planets compared to the "disruptive" force of the outer planet. If $\epsilon \gg 1$ ($\nu_{cd} - \nu_{bd} \gg \nu_{bc} + \nu_{cb}$), $\hat{l}_b$ and $\hat{l}_c$ will be forced apart by

their different precession rates around planet d and thereby acquire relatively large mutual inclinations. In this case, their maximum mutual inclination will be two times the inclination of outer planet i_d ($i_{bc,\max} = 2i_d$) (Lai & Pu 2017). Conversely, if $\epsilon \ll 1$ ($\nu_{cd} - \nu_{bd} \ll \nu_{bc} + \nu_{cb}$), the two inner planets will strongly couple and precess around Kepler-129 d together. In the condition of $\epsilon \ll 1$, their maximum mutual inclination can be given by the product of ϵ and $\sin(2i_d)$ ($|\sin(i_{bc,\max})| = \epsilon|\sin 2i_d|$) (Lai & Pu 2017).

For the Kepler-129 planets, we find $\nu_{bc} \approx 24 \deg \mathrm{kyr}^{-1}$, $\nu_{bd} \approx 1.4 \deg \mathrm{kyr}^{-1}$, $\nu_{cb} \approx 2.5 \deg \mathrm{kyr}^{-1}$, and $\nu_{cd} \approx 7.4 \deg \mathrm{kyr}^{-1}$. As $\nu_{bc} + \nu_{cb}$ is nearly 4.5 times larger than $\nu_{cd} - \nu_{bd}$, this indicates that Kepler-129 b and c precess around Kepler-129 d together while keeping a relatively small mutual inclination. Here, we obtained a rough estimate of $i_{bc,\max} \sim 8°$ if the outer giant planet is inclined by 19° relative to inner planets.

5.2. N-body Simulation

5.2.1. Simulation Setup

We present the analytical model that an inclined outer giant planet can cause the spin–orbit misalignment of two inner planets in Section 5.1.1. But the mutual inclination between Kepler-129 d and inner planets cannot be determined with only RV observations due to the degeneracy between the true mass and inclination of Kepler-129 d. In this section, we performed N-body simulations to set constraints on the inclination between the inner planets and the outer giant planet.

The numerical integrations are carried out using the N-body package *REBOUND* (Rein & Liu 2012). We use the stellar mass and radius from Silva Aguirre et al. (2015) for the simulation setup. The initial conditions of planets (m_c, $m \sin i_d$, a_d, e_d, ω_d) are drawn from the MCMC posterior samples obtained in Section 3 (see Table 2). For Kepler-129 b, we drew m_b from a Gaussian distribution that is centered at the predicted mass given by mass–radius relation in Weiss & Marcy (2014) and 3σ below the measured upper limit ($\mu = 1.38\,M_\oplus$, $\sigma = 0.4\,M_\oplus$). We set $a_b = 0.13$ au, $a_c = 0.39$ au based on transit observations (Van Eylen & Albrecht 2015). We also set their eccentricities and argument of pericenter (e_b, e_c, ω_b, ω_c) to 0 since transit observations show both planet b and c are consistent with having zero eccentricity (Van Eylen & Albrecht 2015). Assuming Kepler-129 b and c are nearly coplanar in the beginning, we drew the initial mutual inclination between Kepler-129 b and c from a Rayleigh distribution with a width of 1°.5 (Fabrycky et al. 2014) and set their initial longitude of ascending node Ω to zero. We did not use the inclinations from transit observations because the published impact parameters tend to be poorly constrained and highly degenerate with eccentricities and limb darkening models. Furthermore, it is not essential to begin our simulations with the exact values of the inclinations that the planets currently have because the mutual inclinations of the planets evolve with time. The simulations are divided into six samples, which have initial mutual inclinations between the outermost inner planet and the giant $i_{cd,0}$ as 5°, 10°, 15°, 20°, 25°, 30°. We repeated 1000 trials for each sample, which amounts to 6000 simulations in total, and run every simulation for 200 kyr.

5.2.2. Inclination Oscillation of Inner Planets

We show the orbital evolution of three planets in the left panel of Figure 8, which is a polar plot where the radical
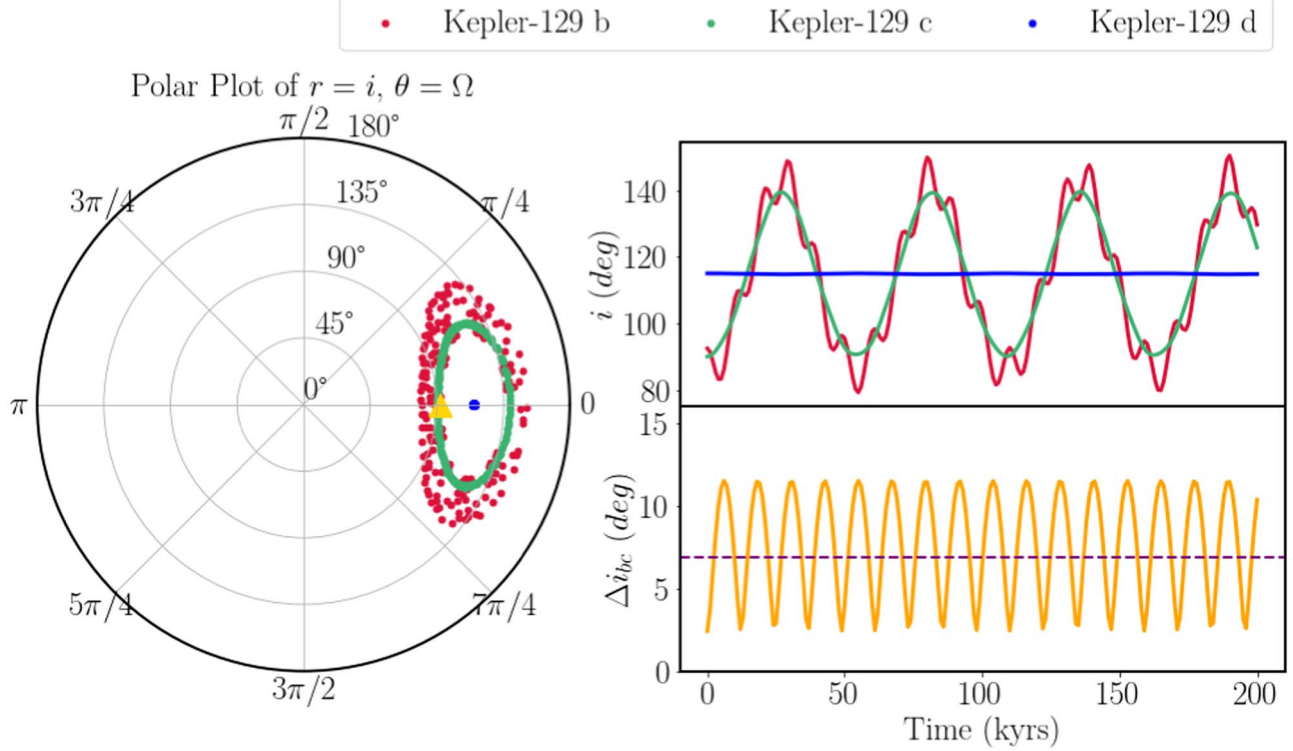
Figure 8. An example of the dynamical evolution in Kepler-129 from our N-body simulations. The simulation setup is: $m_b = 3.4\ M_\oplus$, $m_c = 47\ M_\oplus$, $m_d = 8.3\ M_{\rm Jup}$, $a_d = 4$ au, $i_{cd,0} = 25°$, $i_{bc,0} = 2°\!.4$. The initial mutual inclination between planet b and c is drawn from a Rayleigh distribution with a width of $1°\!.5$. Left: polar plot of $r = i$ (inclination), $\theta = \Omega$ (longitude of ascending node). The orbit of Kepler-129 d is nearly invariant (blue), whereas Kepler-129 b (red) and c (green) both precess around Kepler-129 d. As Kepler-129 b and c precess, their inclinations oscillate between the initial value ($\sim 90°$, marked by the yellow triangle) and $\sim 150°$. In the meantime, Kepler-129 b precesses around Kepler-129 c at a much faster rate, which shows up as short-period variations in the red trajectory. Top right: inclination of the three planets as a function of time. Bottom right: mutual inclination between planet b and c Δi_{bc} change as a function of time. Kepler-129 b and c both remain in a transiting configuration if Δi_{bc} is below the threshold ($6°\!.9$) marked by the purple dashed line.

coordinate is inclination ($r = i$) and the angular coordinate is the longitude of ascending node ($\theta = \Omega$). The overall behavior matches the predictions of the analytical model in Section 5.1. First, the location of Kepler-129 d (blue points) stays nearly constant, indicating its orbit is approximately invariant during the entire simulation. Second, the orbits of Kepler-129 b (red) and c (green) trace cyclical trajectories around Kepler-129 d, suggesting they precess around the orbital axis of Kepler-129 d together. These are consistent with the analytical argument that Kepler-129 d contains much more angular momentum than Kepler-129 b and c ($\nu_4 \ll \nu_3$), so the orbit of Kepler-129 d is hardly influenced while Kepler-129 b and c precess around Kepler-129 d together. During the precession, the inclination of Kepler-129 b and c oscillate as a function of time with a period of ~ 54 kyr (also see top-right panel of Figure 8). This timescale is close to the analytic estimate in Section 5.1.1 ($2\pi/\nu_3 \approx 52$ kyr). In addition, Kepler-129 b also precesses around Kepler-129 c at a faster rate, which appears as shorter-period variations in the red trajectory. The behavior is predicted when we consider angular momenta of Kepler-129 b and c separately in Section 5.1.2. This short period of ~ 12 kyr is also consistent with the precession period of Kepler-129 b around Kepler-129 c estimated in Section 5.1.2 ($2\pi/\nu_{bc} \approx 15$ kyr).

5.2.3. Double-transit Probability

In order to quantify whether the simulated inner planets transit together as observed, we define the parameter double-transit pprobability (DTP) for Kepler-129 b and c (e.g., Becker & Adams 2017; Read et al. 2017). DTP is the fraction of time

when two inner planets can both be observed to transit from any line of sight along their mutual ecliptic. This occurs when their mutual inclination is lower than a threshold $\Delta i_{\rm max} = \arctan(R_\star/a_b) + \arctan(R_\star/a_c)$. The two planets attain $\Delta i_{\rm max}$ in the extreme scenario where they present grazing transits in two different hemispheres of the host star. Note that this definition does not assume a specific line of sight, e.g., from Earth. We still consider planets to be both transiting if they can been seen from another line of sight, but not from Earth's line of sight. In our case, $\Delta i_{\rm max} = 6°\!.9$ for Kepler-129 b and c, as marked by the dashed line in the bottom right panel of Figure 8. For each of our simulations, we calculated DTP as the fraction of time when $\Delta i_{bc} < \Delta i_{\rm max} = 6°\!.9$, where Δi_{bc} is the mutual inclination between planet b and c.

DTP depends on the architecture of the system. For example, Becker & Adams (2017) found that exterior perturbers with smaller periastron distances are more likely to disturb compact inner planets and excited them out of a mutually transiting configuration. In our case, we constrain the orbital elements of three planets from observations in Section 3.2 and Van Eylen & Albrecht (2015; see Table 2). One missing but important element of the system is the mutual inclination between planets. Hence we vary the initial mutual inclination between the outermost transiting planet Kepler-129 c and the giant planet Kepler-129 d ($i_{cd,0}$) from $5°$–$30°$ to explore its effect on DTP. In turn, we get a constrain on the $i_{cd,0}$ based on DTP. Here, $i_{cd,0}$ is approximately the initial inclination between the inner planetary system and Kepler-129 d since planets b and c are almost coplanar in the beginning of the simulation. Note
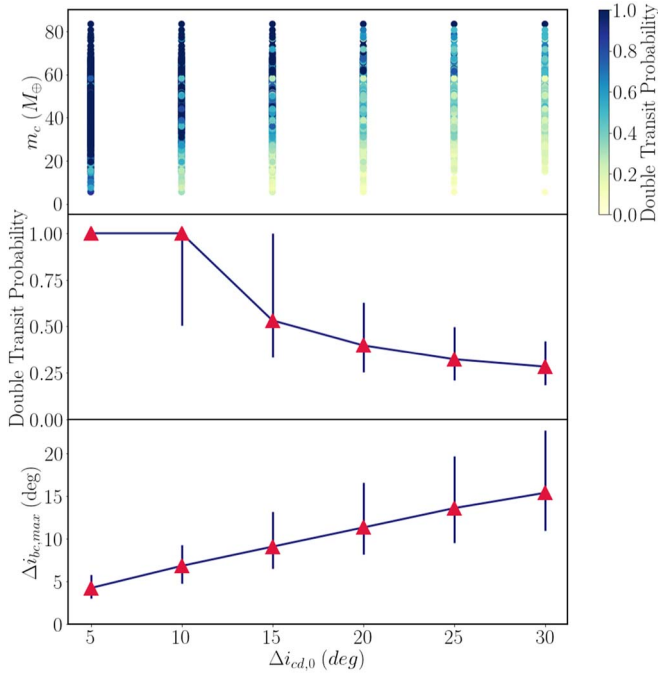
Figure 9. Mutual inclination between Kepler-129 b and c increases, and thus the DTP of them decreases as the misalignment between inner and outer planets rises. Top: DTP of simulations with an initial mutual inclination between Kepler-129 c and d ($\Delta i_{cd,0}$) ranging from 5°–30°. The mass of Kepler-129 c m_c is drawn from the MCMC posterior distribution obtained in Section 3.2. Middle and bottom: median value of the DTP and $\Delta i_{bc,\max}$ of samples with the same $\Delta i_{cd,0}$ in the top panel, with error bars corresponding to the 1σ confidence interval. When $i_{cd,0} = 5°$, $\Delta i_{bc,\max}$ is around 4°, rising linearly to $i_{bc,\max} = 15°$ when $\Delta i_{cd,0} = 30°$. Accordingly, the DTP decreases as $\Delta i_{cd,0}$ increases. Here, the inner planets will be observed as both transiting ∼40% of time if $\Delta i_{cd,0} = 20°$ and less than ∼28% of time if $\Delta i_{cd,0} = 30°$. In addition, at a given $\Delta i_{cd,0}$, the DTP increases as m_c increases, indicating that a Kepler-129 c enables stronger coupling between the inner planets which helps to resist perturbations from Kepler-129 d.

that we limit $i_{cd,0}$ to below 30° to avoid Kozai–Lidov oscillations that can cause the inclination and eccentricity of inner planets to attain high values, and may even destabilize their orbits.

In the top panel of Figure 9, we plot DTP against $i_{cd,0}$ and the mass of Kepler-129 c m_c. In the middle and bottom panel, we plot the median value and 1σ confidence interval of DTP and $i_{bc,\max}$ of samples with the same $i_{cd,0}$ in the top panel. The dispersion in DTP is largely from the different values of m_c, which were drawn from posteriors of the RV fit. Overall, DTP decreases with increasing $i_{cd,0}$ because a more inclined perturber imposes a larger torque on the inner planets and excites larger mutual inclinations between them. When $i_{cd,0} < 10°$, DTP is equal to or around one, implying that the coplanarity of Kepler-129 b and c is not disturbed if the outer giant planet is inclined by less than 10° relative to them. In Section 5.1.1, we found that the spin–orbit angle $> \sim 38°$ between the inner planets and the stellar spin requires at least ∼19° of misalignment between the inner planetary system and outer giant planet. Our results shows that the probability of observing the simultaneous transits of Kepler-129 b and c is ∼40% when $\Delta i_{cd,0} = 20°$. If $\Delta i_{cd,0} = 30°$, Kepler-129 b and c will remain in double-transit configuration less than 28% of the time, making them less likely to be observed as cotransiting.

In the analysis of Section 5.1.2, we concluded that the orbital evolution of Kepler-129 b and c are determined by two effects:

the separating "force" due to perturbations from Kepler-129 d and the coupling "force" due to their mutual precession around each other. In our simulations, we found a consistent result: DTP increases as the mass of Kepler-129 c (m_c) increases. Specifically, a more massive Kepler-129 c imposes a larger gravitational influence on Kepler-129 b and makes Kepler-129 b precess around planet c's angular momentum vector faster. In this way, the dynamical coupling between Kepler-129 b and c is stronger, making it more difficult for the giant planet to excite mutual inclinations between the inner planets.

In conclusion, we found that the mutual inclination between inner planets and the outer giant planet should be larger than 19° to produce the measured ∼38° spin–orbit angle. But when the mutual inclination between inner planets and the outer giant planet is larger than 30°, the probability that Kepler-129 b and c both remain in transit configuration is smaller than 28%.

6. Discussion

6.1. Comparison to Other Planetary Systems

Several exoplanets systems that host spin–orbit misaligned close-in small planets have been found to contain an distant giant planet, e.g., HAT-P-11 (Winn et al. 2010; Yee et al. 2018), π Men (Jones et al. 2002; Kunovac Hodžić et al. 2021), Kepler-56 (Huber et al. 2013; Otor et al. 2016), and WASP-107 (Piaulet et al. 2021; Rubenzahl et al. 2021). Kepler-129 joins their ranks. HAT-P-11, π Men, and WASP-107 host single transiting planets, whereas Kepler-56 and Kepler-129 host two dynamically coupled transiting planets. In both HAT-P-11 and π Men, the outer giant planets are highly inclined relative to the inner planets (∼50°) and have high eccentricities (∼0.6) (Xuan & Wyatt 2020). On the contrary, the giant planets in Kepler-56 and Kepler-129 have moderate eccentricities (0.21 and 0.15, respectively). This current sample is consistent with the scenario that more eccentric and inclined perturbers could possibly excite some of the inner planets out of a transiting configuration, resulting in lower transit multiplicities. Furthermore, the outer transiting planets in Kepler-56 and Kepler-129 both have relatively high masses (Kepler-56 c ∼ 195 $M_\oplus$ and Kepler-129 c ∼ 43 $M_\oplus$), which enables strong coupling between themselves and the inner transiting planets. This effect suppresses the excitation of mutual inclinations between the two transiting planets from the outer giant.

6.2. Possible Mechanisms to Cause the Spin–Orbit Misalignment

We have discussed how an inclined giant planet could perturb the orbits of inner planets and cause their orbits to be misaligned with the stellar spin axis. But what gives the mutual inclination between the inner and outer planets in these systems? One possible scenario is that all planets form in the protoplanetary disk and are aligned with each other. At some point, two or more giant planets underwent dynamical encounters and only one giant planet remains, which ends up with a high eccentricity and high-inclination orbit relative to the initial disk plane (Chatterjee et al. 2008). The giant planets in HAT-P-11 and π Men are consistent with this mechanisms with high eccentricities and high inclinations. An alternative possibility is that the planets formed in a warped protoplanetary disk with misaligned inner and outer components (Nealon et al. 2019; Xuan & Wyatt 2020). In this scenario, the inner and outer planets could be misaligned with each other from the

beginning. The two scenarios are both possible for Kepler-129 system. Since the planet–planet scattering may produce relatively high eccentricities for the remaining giant planets whereas a warped protoplanetary disk does not, more discoveries of such systems in the future can help to study the eccentricities distribution of the outer giant planets statistically and distinguish the two possibilities.

Several other mechanisms can also explain the spin–orbit misalignment. One possibility is that the stellar spin was initially misaligned with respect to the protoplanetary disk. In this case, the inner planets may be misaligned with the stellar spin when they formed. Hjorth et al. (2021) found two coplanar transiting planets' orbits are retrograde with respect to the host star (K2-290A) in a triple system, indicating the protoplanetary disk was misaligned due to perturbations from the neighboring star. Spalding & Batygin (2014) and Spalding & Millholland (2020) argue that the quadrupolar gravitational potential of a tilted, rapidly rotating host star would torque the orbits of close-in planets. Because Kepler-129 has already evolved into the subgiant stage and rotates relatively slowly, it is more likely that the influence of Kepler-129 vanishes as it spins down.

6.3. Opportunities for Future Observation

Our RV baseline is too short to cover a full orbital period of Kepler-129 d. Future RV monitoring will provide a better constraint on the orbital period and minimum mass of Kepler-129 d. In addition, more RV data would enable more precise masses for Kepler-129 b and c. The Transiting Exoplanet Survey Satellite (TESS) has the potential to reveal more transiting planets and its short cadence data can also be used to measure spin–orbit angles with asteroseismology for other planetary systems (TESS will not be able to detect oscillations for Kepler-129 since it is too faint). Combining results from TESS and long-baseline RV observations could help us uncover other systems like Kepler-129 and study the influence of outer giant planets on small inner planets on a statistical level.

7. Conclusion

We have presented the discovery of a long-period giant planet Kepler-129 d outside two known transiting sub-Neptune-sized planets Kepler-129 b and c, and studied the orbital dynamics of the system. Our main conclusions are as follows:

1. Kepler-129 hosts two known transiting planets Kepler-129 b ($P_b = 15.79$ days, $r_b = 2.40 \pm 0.04\, R_\oplus$) and Kepler-129 c ($P_c = 82.20$ days, $r_c = 2.52 \pm 0.07\, R_\oplus$). We constrain the masses of Kepler-129 b and c with RV observations: $m < 20\, M_\oplus$, $m = 43^{+13}_{-12}\, M_\oplus$.

2. Kepler-129 d is a long-period giant planet with moderate eccentricity ($P_d = 7.2^{+0.4}_{-0.3}$ yr, $e_d = 0.15^{+0.07}_{-0.05}$) outside the compact inner system. Kepler-129 d is a massive planet ($m \sin i_d = 8.3^{+1.1}_{-0.7}\, M_{\rm Jup}$), whose minimum mass is close to the traditional boundary between planets and brown dwarfs. The true mass of Kepler-129 d may be larger due to the unknown inclination so we cannot rule out the possibility that it is a brown dwarf.

3. Kepler-129 is a subgiant star with a clear presence of oscillation modes. From our best-fit models to the stellar oscillations, we found that the angle between stellar spin axis and line of sight to be $i_s = 52^{+10}_{-13}$ deg. Assuming Kepler-129 b and c have edge-on orbits, the spin–orbit angle of inner planets is $>39°$.

4. The spin–orbit misalignment of Kepler-129 b and c indicates that their orbits may have been tilted via nodal precession around a misaligned Kepler-129 d. This scenario requires a mutual inclination between the inner planetary system and Kepler-129 d of at least $19°$.

5. *N*-body simulations show Kepler-129 b and c both remain transiting 40% of the time if they are inclined by $20°$ relative to Kepler-129 d. This due to the relatively strong coupling between the two inner planets. However, if their inclination relative to Kepler-129 d rises to $30°$ then Kepler-129 b and c will be observed to transit together only 28% of the time.

Appendix

We present the MCMC fitting reults of RV data below (see
Figure 10).
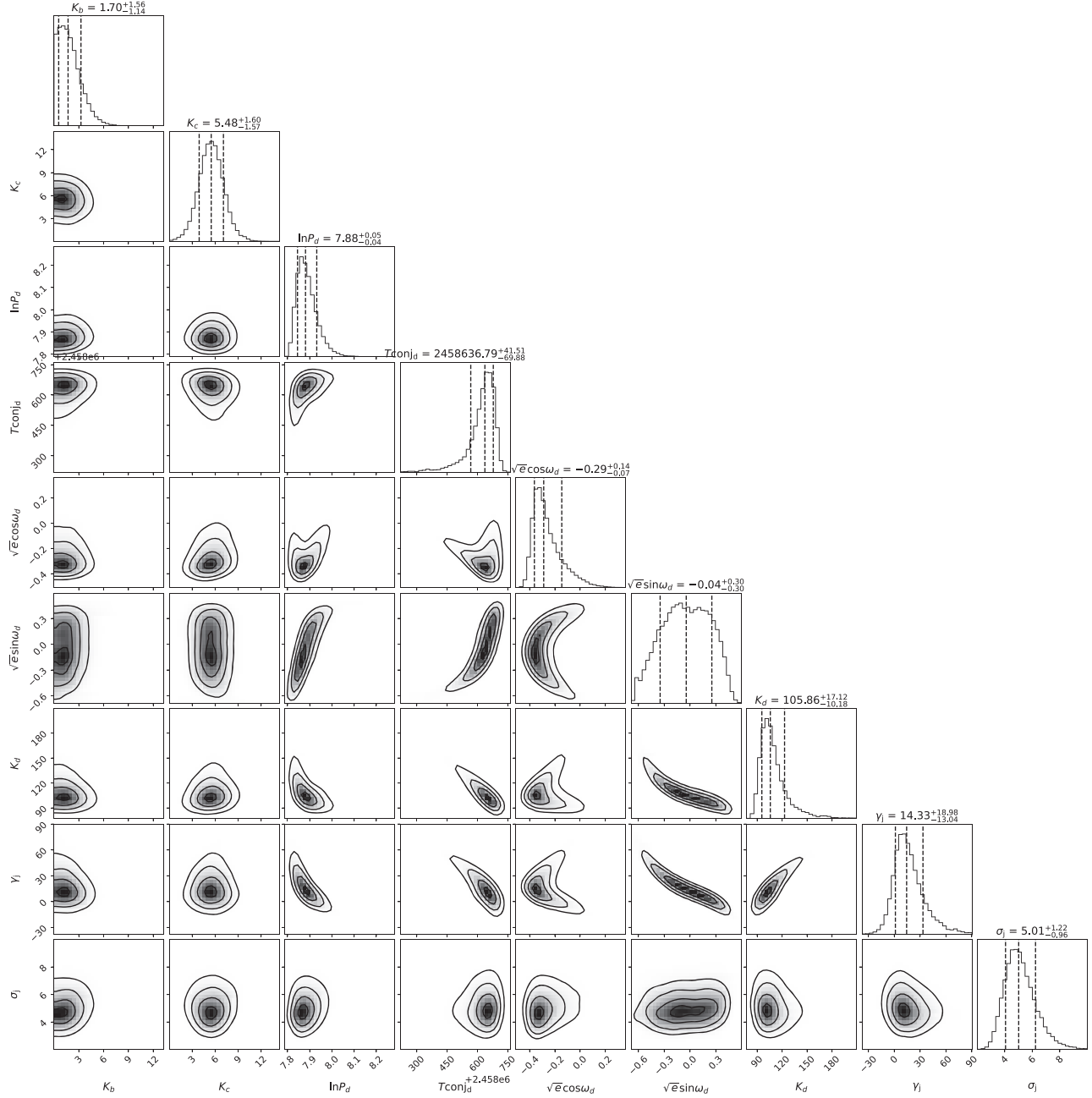
Figure 10. Joint posterior distributions for Kepler-129 b, c, and d's orbital parameters (P_d, K_d, e_d, ω_d, tc_d, K_b, K_c, γ, σ) using the MCMC method. Moving forward, the solid lines correspond to 1σ, 2σ, and 3σ contours.

ORCID iDs

Jingwen Zhang (张婧雯) ● https://orcid.org/0000-0002-2696-2406

Lauren M. Weiss ● https://orcid.org/0000-0002-3725-3058

Daniel Huber ● https://orcid.org/0000-0001-8832-4488

Sarah Blunt ● https://orcid.org/0000-0002-3199-2888

Ashley Chontos ● https://orcid.org/0000-0003-1125-2564

Benjamin J. Fulton ● https://orcid.org/0000-0003-3504-5316

Samuel Grunblatt ● https://orcid.org/0000-0003-4976-9980

Andrew W. Howard ● https://orcid.org/0000-0001-8638-0320

Howard Isaacson ● https://orcid.org/0000-0002-0531-1073

Molly R. Kosiarek ● https://orcid.org/0000-0002-6115-4359

Erik A. Petigura ● https://orcid.org/0000-0003-0967-2893

Lee J. Rosenthal ● https://orcid.org/0000-0001-8391-5182

Ryan A. Rubenzahl ● https://orcid.org/0000-0003-3856-3143

References

Armstrong, D. J., Lopez, T. A., Adibekyan, V., et al. 2020, Natur, 583, 39
Ballot, J., Appourchaux, T., Toutain, T., & Guittet, M. 2008, A&A, 486, 867
Ballot, J., García, R. A., & Lambert, P. 2006, MNRAS, 369, 1281
Becker, J. C., & Adams, F. C. 2017, MNRAS, 468, 549
Boué, G., & Fabrycky, D. C. 2014a, ApJ, 789, 110
Boué, G., & Fabrycky, D. C. 2014b, ApJ, 789, 111
Boué, G., & Laskar, J. 2006, Icar, 185, 312
Boué, G., & Laskar, J. 2009, Icar, 201, 750
Bourrier, V., Lovis, C., Beust, H., et al. 2018, Natur, 553, 477
Bowler, B. P., Blunt, S. C., & Nielsen, E. L. 2020, AJ, 159, 63
Campante, T. L., Handberg, R., Mathur, S., et al. 2011, A&A, 534, A6
Campante, T. L., Lund, M. N., Kuszlewicz, J. S., et al. 2016, ApJ, 819, 85
Chaplin, W. J., & Miglio, A. 2013, ARA&A, 51, 353
Chaplin, W. J., Sanchis-Ojeda, R., Campante, T. L., et al. 2013, ApJ, 766, 101
Chatterjee, S., Ford, E. B., Matsumura, S., & Rasio, F. A. 2008, ApJ, 686, 580
Collier Cameron, A., Bruce, V. A., Miller, G. R. M., Triaud, A. H. M. J., & Queloz, D. 2010, MNRAS, 403, 151
Damasso, M., Sozzetti, A., Lovis, C., et al. 2020, A&A, 642, A31
de Laplace, P. S. 1796, Exposition du Système du Monde (Charleston, SC: Nabu Press)
De Rosa, R. J., Dawson, R., & Nielsen, E. L. 2020, A&A, 640, A73
Denham, P., Naoz, S., Hoang, B.-M., Stephan, A. P., & Farr, W. M. 2019, MNRAS, 482, 4146
Díaz, M. R., Jenkins, J. S., Feng, F., et al. 2020, MNRAS, 496, 4330
Dziembowski, W. 1977, AcA, 27, 203
Fabrycky, D. C., Lissauer, J. J., Ragozzine, D., et al. 2014, ApJ, 790, 146
Fabrycky, D. C., & Winn, J. N. 2009, ApJ, 696, 1230
Foreman-Mackey, D., Hogg, D. W., Lang, D., & Goodman, J. 2013, PASP, 125, 306
Fulton, B. J., & Petigura, E. A. 2018, AJ, 156, 264
Fulton, B. J., Petigura, E. A., Blunt, S., & Sinukoff, E. 2018, PASP, 130, 044504
Gizon, L., & Solanki, S. K. 2003, ApJ, 589, 1009
Grossman, A. S., & Graboske, H. C. 1973, ApJ, 180, 195
Hekker, S., Barban, C., Baudin, F., et al. 2010, A&A, 520, A60
Hirano, T., Narita, N., Shporer, A., et al. 2011, PASJ, 63, 531
Hjorth, M., Albrecht, S., Hirano, T., et al. 2021, PNAS, 118, 2017418118
Howard, A. W., Johnson, J. A., Marcy, G. W., et al. 2010, ApJ, 721, 1467
Huang, C. X., Petrovich, C., & Deibert, E. 2017, AJ, 153, 210
Huber, D., Carter, J. A., Barbieri, M., et al. 2013, Sci, 342, 331
Jones, H. R. A., Paul Butler, R., Tinney, C. G., et al. 2002, MNRAS, 333, 871
Kamiaka, S., Benomar, O., & Suto, Y. 2018, MNRAS, 479, 391
Kamiaka, S., Benomar, O., Suto, Y., et al. 2019, AJ, 157, 137
Kant, I. 1755, Allgemeine Naturgeschichte und Theorie des Himmels (Lefkosia: TP Verone Publishing)
Kunovac Hodžić, V., Triaud, A. H. M. J., Cegla, H. M., Chaplin, W. J., & Davies, G. R. 2021, MNRAS, 502, 2893
Lai, D., & Pu, B. 2017, AJ, 153, 42
Landin, N. R., Mendes, L. T. S., & Vaz, L. P. R. 2009, A&A, 494, 209
Ledoux, P. 1951, ApJ, 114, 373
Lightkurve Collaboration, Cardoso, J. V. D. M., Hedges, C., et al. 2018, Lightkurve: Kepler and TESS Time Series Analysis in Python, Astrophysics Source Code Library, ascl:1812.013
Lopez, E. D., & Fortney, J. J. 2014, ApJ, 792, 1
Lund, M. N., Silva Aguirre, V., Davies, G. R., et al. 2017, ApJ, 835, 172
Masuda, K., Winn, J. N., & Kawahara, H. 2020, AJ, 159, 38
McLaughlin, D. B. 1924, ApJ, 60, 22
Nealon, R., Pinte, C., Alexander, R., Mentiplay, D., & Dipierro, G. 2019, MNRAS, 484, 4951
Otor, O. J., Montet, B. T., Johnson, J. A., et al. 2016, AJ, 152, 165
Petigura, E. A. 2015, PhD thesis, University of California, Berkeley
Piaulet, C., Benneke, B., Rubenzahl, R. A., et al. 2021, AJ, 161, 70
Pu, B., & Lai, D. 2018, MNRAS, 478, 197
Read, M. J., Wyatt, M. C., & Triaud, A. H. M. J. 2017, MNRAS, 469, 171
Rein, H., & Liu, S. F. 2012, A&A, 537, A128
Rossiter, R. A. 1924, ApJ, 60, 15
Rowe, J. F., Bryson, S. T., Marcy, G. W., et al. 2014, ApJ, 784, 45
Rubenzahl, R. A., Dai, F., Howard, A. W., et al. 2021, AJ, 161, 119
Scargle, J. D. 1982, ApJ, 263, 835
Schlaufman, K. C. 2018, ApJ, 853, 37
Silva Aguirre, V., Davies, G. R., Basu, S., et al. 2015, MNRAS, 452, 2127
Spalding, C., & Batygin, K. 2014, ApJ, 790, 42
Spalding, C., & Millholland, S. C. 2020, AJ, 160, 105
Van Eylen, V., & Albrecht, S. 2015, ApJ, 808, 126
Vandakurov, Y. V. 1967, AZh, 44, 786
Vogt, S. S., Allen, S. L., Bigelow, B. C., et al. 1994, Proc. SPIE, 2198, 362
Weiss, L. M., & Marcy, G. W. 2014, ApJL, 783, L6
Winn, J. N., Johnson, J. A., Howard, A. W., et al. 2010, ApJL, 723, L223
Winn, J. N., Noyes, R. W., Holman, M. J., et al. 2005, ApJ, 631, 1215
Xie, J.-W. 2014, ApJS, 210, 25
Xuan, J. W., & Wyatt, M. C. 2020, MNRAS, 497, 2096
Yee, S. W., Petigura, E. A., Fulton, B. J., et al. 2018, AJ, 155, 255
Zanazzi, J. J., & Lai, D. 2018, MNRAS, 477, 5207
Zeng, L., & Seager, S. 2008, PASP, 120, 983